Journal of Materials Chemistry C

ROYAL SOCIETY OF CHEMISTRY

PAPER

View Article Online
View Journal

Cite this: DOI: 10.1039/d5tc03013g

Exploring the gas-sensing properties at room-temperature and electrical behavior of oxalyldihydrazide-derived molybdenum complexes

Josipa Sarjanović,[a] Marta Razum,[b] Béla Fiser,[cde] Luka Pavić *[b] and Jana Pisk *[a]

This study reports the design, synthesis, characterization, and performance evaluation of novel semiconductive molybdenum coordination complexes derived from an oxalyldihydrazide-based ligand. The ligand H_4L was synthesized through the reaction of salicylaldehyde with oxalyldihydrazide, followed by coordination with a molybdenum metal center. From methanol solution, a dinuclear complex, $[Mo_2O_4(L)(MeOH)_2]\cdot 2H_2O$, was isolated, while a polynuclear complex of the formula $[Mo_2O_4(L)]_n$ was obtained from ethanol, acetonitrile, or acetone. These complexes were characterized using spectroscopic techniques and elemental analysis, and their thermal stabilities were assessed using thermogravimetric analysis. Density functional theory calculations were used to further assess the structural properties. The crystal and molecular structures of $[Mo_2O_4(L)(MeOH)_2]\cdot 2MeOH$ were determined through single-crystal X-ray diffraction. Notably, the materials exhibited moderate DC conductivity of $4.27 \times 10^{-8}\ \Omega^{-1}\ cm^{-1}$ for $[Mo_2O_4(L)]_n$ and $1.59 \times 10^{-9}\ \Omega^{-1}\ cm^{-1}$ for $[Mo_2O_4(L)(MeOH)_2]\cdot 2H_2O$@200 °C. $[Mo_2O_4(L)(MeOH)_2]\cdot 2H_2O$ demonstrated potential applicability for the detection of volatile organic compounds (VOCs), including MeOH, EtOH, and PrOH, as well as H_2O. Specifically, exposure to MeOH led to a six-order magnitude increase in conductivity, highlighting its high sensitivity. Exposure to EtOH resulted in a five-order magnitude increase, whereas exposure to PrOH led to a four-and-a-half-order magnitude increase in conductivity. Further optimization of the experimental setup enabled reproducible response cycles upon exposure of the material to methanol vapor. Moreover, the response time for MeOH detection was as low as 40 s, with a recovery time of 230 s, indicating high sensing efficiency at RT.

Received 9th August 2025,
Accepted 1st December 2025

DOI: 10.1039/d5tc03013g

rsc.li/materials-c

Introduction

Industry 4.0 compiles ground-breaking technologies to revolutionise production landscapes. Technological advancements in sensor expertise, big data, cloud computing, artificial intelligence, robotics, and automated control systems pave the way for intelligent plants and smart manufacturing. Sensors play a pivotal role in enhancing product quality, reducing production costs, and providing new market opportunities, enabling rapid, precise data fluctuation and communication by transforming traditional manufacturing processes.[1,2] A sensor detects and measures input stimuli such as pressure, force, flow, light, heat, motion, and moisture. These stimuli are converted into measurable digital signals, typically electrical outputs such as current, voltage, capacitance, resistance, or frequency. A signal can be displayed for interpretation or transmitted over a network for further processing. Sensors bridge the gap between the physical world and digital systems, enabling data collection and analysis in various applications. Gas sensors find diverse applications, including breath analysis for medical diagnostics, smart home systems, industrial safety, air pollution monitoring, and alcohol detection. Applications such as infrared (IR) gas sensors,[3] quartz crystal microbalances,[4] surface acoustic wave devices,[5] gas chromatographs,[6] calorimetric sensors,[7] and solid-state sensors[8] have contributed to their evolution. Solid-state sensors, specifically metal oxide semiconductors (MOSs), conducting polymers, metal nanowires, and carbon-based

[a] Department of Chemistry, Faculty of Science, University of Zagreb, Horvatovac 102a, 10000 Zagreb, Croatia. E-mail: jana.pisk@chem.pmf.hr
[b] Division of Materials Chemistry, Ruđer Bošković Institute, Bijenička 54, 10000 Zagreb, Croatia. E-mail: luka.pavic@irb.hr
[c] Institute of Chemistry, University of Miskolc, 3515 Miskolc-Egyetemváros, Hungary
[d] Ferenc Rakoczi II Transcarpathian Hungarian College of Higher Education, 90200 Beregszász, Transcarpathia, Ukraine
[e] Department of Physical Chemistry, Faculty of Chemistry, University of Lodz, 90-236 Lodz, Poland

materials, are promising next-generation gas sensors owing to their ability to detect charge variations in conductive channel materials.[9–12] The intense emission of volatile organic compounds (VOCs) and the associated environmental concerns[13] have boosted interest in coordination compounds and polymers. There are certain literature limitations regarding transition metal (TM) complexes and their sensor properties, although their role in catalysis,[14,15] magnetism,[16,17] adsorption,[18] and/or proton conduction[19] is undoubtful. Among these, metal-based complexes, such as Ir, were employed as electrochemical sensors for cardiac-troponin I,[20] while Cu(II) and Pt(II) containing tridentate 2,6-*bis*(benzimidazol-2-yl)-4-hydroxypyridine were used for glucose and H_2O_2 detection.[21] Furthermore, Cu(I) coordination complexes have arisen as a promising class of optoelectronic materials due to their low toxicity, cost-effectiveness, and environmentally friendly properties.[22] Moreover, Cu(I) complexes incorporating derivative phosphine ligands have demonstrated oxygen gas sensing capabilities.[23–26]

To evaluate the qualitative and quantitative performances of gas sensors, various performance parameters were defined:[27,28] (i) sensitivity, (ii) selectivity, (iii) response and recovery time, (iv) stability, (v) operating temperature, and (vi) limit of detection. An ideal gas sensor should exhibit high sensitivity and selectivity, rapid response and recovery times, long-term stability, operating at room temperature (RT), and a low detection limit. The development of RT operable sensors is increasingly important for various applications. While significant progress has been made in RT detection of inorganic gases, alcohol vapor sensing at RT remains less explored.

In our recent work,[29–31] we reported the semiconducting properties of TM-Schiff base complexes, specifically those based on Mo and V. Building on this foundation, we focused this research on exploring solid-state transformations and advancing the study of the gas-sensing properties by exposing Mo coordination complexes to methanol, ethanol, propanol and H_2O vapours. The complexes reported here contribute to this growing field by enabling reversible, analyte-specific detection of alcohols and H_2O vapors under ambient conditions, without external activation. To achieve this, we selected Mo complexes derived from oxalyldihydrazide ligands (Scheme 1) as the primary subject of investigation. The synthesis of transition metal complexes derived from oxalyldihydrazide ligands presents a significant challenge due to the rarity of such complexes,[32–37] highlighting their unique and demanding nature in coordination chemistry.

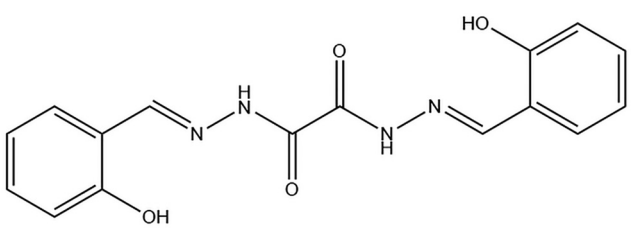

Scheme 1 The ligand H_4L used in the present investigation was obtained through the reaction of salicylaldehyde with oxalyldihydrazide.

The structural and electrical properties of Mo-based coordination complexes are crucial for understanding their stability and reactivity. Density functional theory (DFT) calculations provide valuable insights into these aspects by allowing optimisation of molecular geometries and evaluation of their relative stabilities. These calculations provide a detailed comparison of bonding interactions, hydrogen bonding, and changes in Gibbs free energy, offering a deeper understanding of the experimental observations.

Results and discussion

Synthesis, IR and thermal characterisation of molybdenum(VI) compounds

The H_4L ligand was synthesised through the reaction of oxalyldihydrazide with salicylaldehyde in methanol. DSC data and IR-ATR characterisation are provided in the SI (Fig. S1 and S2). DSC analysis gave information on the melting point and purity of the ligand. For the H_4L ligand, the endothermic peak observed at 314 °C corresponded to melting. The absence of additional peaks confirmed the Schiff base formation. The IR spectrum of the H_4L ligand revealed a characteristic absorption band at 1664 cm^{-1}, corresponding to the C=O stretching vibration, indicative of the keto form of the ligand. Additionally, the band at 1602 cm^{-1} was attributed to the C=N stretching vibration. Bands observed at 3279 and 3200 cm^{-1} were characteristic of O–H stretching vibrations, originating from the salicylaldehyde fragment.[38,39] A high yield of 85% was obtained by solution-based synthesis. Despite the high yield, efforts were made to achieve this reaction through mechanochemical methods to adhere to the principles of green chemistry and eliminate the use of large quantities of methanol.[40,41] The optimised mechanochemical reaction was conducted for 30 minutes at 25 Hz (Table S1).

Reactions between the synthesised ligand H_4L and the molybdenum(VI) precursor $[MoO_2(acac)_2]$ were conducted in various solvents, including methanol, ethanol, acetonitrile, and acetone, in a 1:2 molar ratio. The reaction in methanol resulted in a yellow complex obtained in a solution that turned orange when exposed to air, whereas the reactions in ethanol, acetonitrile, and acetone yielded a brown complex. All the complexes were characterised using TG analysis and IR-ATR (see SI, Fig. S3–S6). The data obtained for the brown complex were all the same, implying that the same compound was obtained, regardless of the solvent used, whereas the data obtained for the orange complex differed. The IR spectrum of the orange complex showed absorption bands at 1599 cm^{-1} and 1595 cm^{-1} for the brown complex, corresponding to C=N (imine) stretching vibrations. Additional bands were observed at 1256 cm^{-1} for the orange complex and at 1222 cm^{-1} for the brown complex, indicative of C–O stretching in phenyl groups,[42,43] implying ligand coordination through ONO atoms. Sharp bands appearing at 898 cm^{-1} and 868 cm^{-1} for the orange complex correspond to O=Mo=O bond stretching, whereas the broad bands at 836 and 810 cm^{-1} for the brown

complex were attributed to the intramolecular stretching of the Mo═O···Mo bond. For the orange complex, a band at 1646 cm^{-1} is observed, which can be attributed to water vibrations, while a band at 1033 cm^{-1} corresponds to the characteristic vibrations of methanol.[44,45] This suggests that methanol and water are likely coordinated with the metal centre or possibly located within voids in the crystal structure. In contrast, the absence of these bands in the spectrum of the brown complex, which aligns with the solvent used during the reaction, may indicate that the brown complex exhibits a polynuclear structure.[29,30]

When heated in an oxygen atmosphere, the orange complex underwent two-step mass loss within a specific temperature range of 50–110 °C, followed by complex decomposition from 350 to 380 °C. In the first step of thermal decomposition, a mass loss of 15.46% was observed, which corresponds to the loss of two water molecules and two methanol molecules. This value aligns closely with a theoretical mass loss of 14.76%. Based on known Mo(VI) Schiff base complexes reported in the literature, the coordination of methanol and water at 6th coordination site is influenced by their donor properties. It is expected that methanol will coordinate preferentially over water due to its comparable donor strength.[45,46] After the second decomposition step, the observed residual mass was 19.47%, closely approximating the theoretical residue for MoO_3 at 21.22%, which is in agreement with the expected composition $[Mo_2O_4(L)(MeOH)_2]\cdot 2H_2O$ (**1**). In contrast, the brown complex displayed a single mass loss step in the range of 375–385 °C. One decomposition step corresponds to the breakdown of a polynuclear complex, yielding a residue of 23.67%. This residue aligns well with the theoretical value for MoO_3 at 24.90%, supporting the presence of molybdenum within the polynuclear complex structure $[Mo_2O_4(L)]_n$ (**2**). The resulting white residue was confirmed to be MoO_3 by comparing its IR-ATR spectrum with that of the commercially available molybdenum(VI) oxide. Heating the dinuclear complex $[Mo_2O_4(L)(MeOH)_2]\cdot 2H_2O$ (**1**) at 145 °C for one hour led to the formation of the polynuclear complex $[Mo_2O_4(L)]_n$ (**2**), as well. Upon cooling to RT, the synthesized polynuclear complex $[Mo_2O_4\ (L)]_n$ (**2**) remained stable and did not revert to its original structure.

The dinuclear complex $[Mo_2O_4(L)(MeOH)_2]\cdot 2MeOH$ (**1***) was initially yellow but turned orange upon brief exposure to air. A suitable yellow crystal allowed for structural analysis, revealing that each Mo centre was bound to one methanol. TG analysis of orange complex (**1**) confirmed the presence of two methanol molecules and two water molecules within the complex implying that the crystal incorporated water upon moisture exposure. The unchanged IR-ATR spectra and TGA/DSC thermal decomposition profiles of the orange complex **1** over a six-month period demonstrated the material's long-term stability under ambient conditions, confirming its reliability for extended storage and use (SI, Fig. S7 and S8).

Recognizing the complex's responsiveness to environmental conditions, $[Mo_2O_4(L)(MeOH)_2]\cdot 2H_2O$ (**1**) was further exposed to different solvent vapours, methanol (MeOH), ethanol (EtOH), propanol (PrOH), and water (H_2O) vapours for 24 hours, followed by analysis using IR-ATR spectroscopy (Fig. 1 and SI, Fig. S9–S14). Upon exposure to MeOH vapours, the orange complex $[Mo_2O_4(L)(MeOH)_2]\cdot 2H_2O$ (**1**) reverted to its yellow form, with the IR-ATR spectrum showing the disappearance of the H_2O-related absorption band at 1644 cm^{-1} and the presence of only MeOH bands at 1026 cm^{-1}. Exposure to EtOH vapours resulted in a light orange colour, with the IR-ATR spectrum revealing the absence of H_2O and MeOH bands at 1647 and 1030 cm^{-1}, and the appearance of the EtOH-related band at 1035 cm^{-1}. PrOH vapours induced an intense orange colour change, with the corresponding PrOH band at 1061 cm^{-1} in the IR-ATR spectrum, and no evidence of H_2O or MeOH bands. No colour change or IR-ATR change was observed after exposure to H_2O vapours. After the conversion of the complex based on the vapours it was exposed to, the samples were left outside of alcohol and H_2O vapours for 24 hours. Only the complex exposed to MeOH vapours reverted to dinuclear complex $[Mo_2O_4(L)(MeOH)_2]\cdot 2H_2O$ (**1**), while the rest remained stable. This indicates that upon exposure to MeOH vapours, complex **1** transforms into a MeOH-coordinated complex devoid of H_2O molecules, presumably $[Mo_2O_4(L)(MeOH)_2]\cdot 2MeOH$ (**1***). Similarly, exposure to EtOH and PrOH vapours results in the formation of EtOH- and PrOH-coordinated complexes, respectively. However, exposure to H_2O vapours did not induce any structural changes in complex **1** in the solid state.

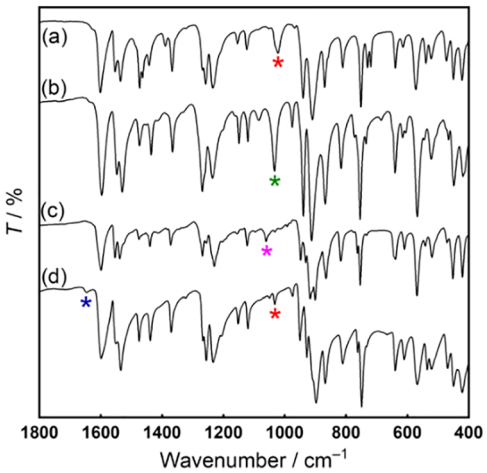

Fig. 1 Comparison of IR ATR spectra after exposure of the dinuclear complex $[Mo_2O_4(L)(MeOH)_2]\cdot 2H_2O$ (**1**) to (a) MeOH, (b) EtOH, (c) PrOH, and (d) H_2O vapours (red – MeOH vibration band, green – EtOH vibration band, purple – PrOH vibration band, and dark blue – water vibration band). The spectrum shown in (d) is the same as that of the starting dinuclear complex $[Mo_2O_4(L)(MeOH)_2]\cdot 2H_2O$ (**1**) before exposure to H_2O vapours.

Crystal and molecular structures

Single-crystal X-ray diffraction (SCXRD) was carried out on crystals obtained directly from the solution. The resulting yellow complex was determined to have the molecular formula $[Mo_2O_4(L)(MeOH)_2]\cdot 2MeOH$ (**1***), see Fig. 2.

The dinuclear compound, $[Mo_2O_4(L)(MeOH)_2]\cdot 2MeOH$ (**1***), crystallizes in the triclinic space group $P\bar{1}$, featuring a unit cell

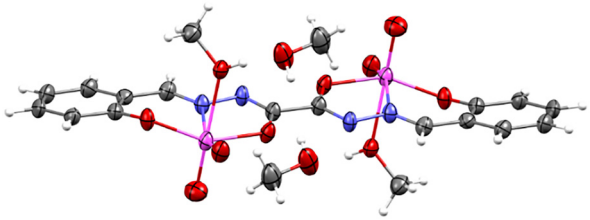

Fig. 2 ORTEP view of $[Mo_2O_4(L)(MeOH)_2]\cdot 2MeOH$ (**1***). The displacement ellipsoids are drawn at 50% probability level at 170 K. Hydrogen atoms are presented as spheres of arbitrary small radii.

that comprises a single molecule of the dinuclear complex $[Mo_2O_4(L)(MeOH)_2]$, along with two molecules of MeOH as solvent inclusions (SI, Table S2). The structure is centrosymmetric, with the inversion centre positioned precisely at the midpoint of the oxalylhydrazonato ligand. Consequently, the complex exhibits a well-defined transconfiguration, aligning with the anticipated stereochemical arrangement of similar dioxomolybdenum(VI) species. Structurally, the $\{MoO_2\}^{2+}$ core is enveloped by an ONO chelating coordination environment, which is attributed to the enolato-imino tautomeric form of the oxalylhydrazonato tetra-anion (SI, Table S3). This tautomeric equilibrium is crucial for stabilizing the coordination geometry and facilitating strong ligand–metal interactions. The 6th coordination site of the Mo(VI) centre is occupied by a MeOH molecule, which engages in a pronounced hydrogen-bonding interaction with an additional, non-coordinated MeOH molecule present in the crystal lattice. A distinctive feature of the crystal packing is the presence of an extensive hydrogen-bonding network that extends beyond the primary coordination sphere. The non-coordinated MeOH molecule plays a key role in propagating this interaction by forming H-bonds with the amide nitrogen atom of an adjacent complex molecule, see the SI, Table S4 and Fig. S15(c). This repetitive hydrogen-bonding motif results in the formation of a supramolecular one-dimensional (1D) chain (SI, Fig. S15(d)), which contributes to the overall stability and structural arrangement of crystals.

Molecular modelling results

The purpose of DFT calculations was to investigate the structural and energetic influence of different solvent molecules (H_2O, MeOH, EtOH, and PrOH) on $[Mo_2O_4(L)(X)_2]\cdot 2X$ complexes, observed through solid-state transformations detailed above. This computational insight complements the experimental findings and provides a molecular-level understanding of the solvent effects on complex stability and geometry.

The crystal structure of $[Mo_2O_4(L)(MeOH)_2]\cdot 2MeOH$ (**1***) was used as the initial structural reference and optimised using the B3LYP/6-31G(d,p)/SDD level of theory with D3 dispersion correction. After verifying that the optimised structure is a real minimum on the potential energy surface, methanol molecules were replaced by water, ethanol and propanol and thus, new complexes were prepared (Table S5). The optimisation was repeated for each case at the same level of theory, and the structures were analysed and compared (Fig. 3).

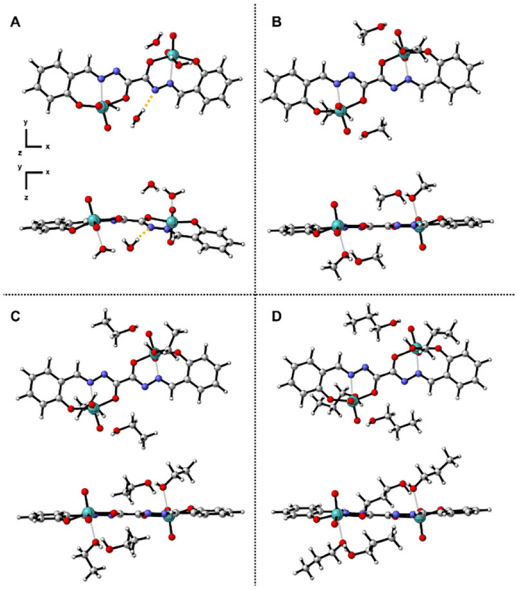

Fig. 3 Optimized structures of $[Mo_2O_4(L)(X)_2]\cdot 2X$ complexes, where X can be H_2O (A), MeOH (B), EtOH (C), or PrOH (D), respectively. An additional hydrogen bond which was formed between water and nitrogen of the ligand is also indicated by an orange dotted line (A).

It was found that the largest deviation occurred in the case of the water-containing complex. It was found that the planar arrangement of $[Mo_2O_4(L)]$ is disrupted (Fig. 3A) in the case of the water-containing complex, while in the case of the alcohol-containing structures it remained more or less similar. By analysing further, the structures including 4 H_2O, MeOH, EtOH, or PrOH and comparing the distances between the directly coordinated oxygen-containing species and Mo, it was observed that the shortest Mo···O is found in the methanol and ethanol complexes (2.441 Å), which is followed by the propanol (2.449 Å) and water (2.459 Å) containing structures, respectively. Although the differences are not large, there is a clear trend which shows that the methanol- and ethanol-containing structures are very similar from a structural and potentially from an electronic point of view. Compared to them, a bit of deviation is experienced in the case of the propanol containing system, and a larger change occurred in the water complex. A similar trend is observed when the hydrogen bond between the two neighbouring oxygen-containing species is analysed. The OH···O distance is increasing by the size of the alcohol (1.656, 1.676, and 1.688 Å for methanol, ethanol, and propanol, respectively), while it is even larger, 1.713 Å, for the water-containing complex.

The relative Gibbs free energies of formation were calculated by using the following equation in which the methanol-containing system was used as a reference:

$$[Mo_2O_4(L)(MeOH)_2]\cdot 2MeOH + 4X \rightarrow [Mo_2O_4(L)(X)_2]\cdot 2X + 4MeOH,$$

where X is water, EtOH or PrOH. It was found that the formation of the ethanol-containing complex is energetically

very close to the methanol system (ΔG = 0.0 kJ mol^{-1}). This is in good agreement with the experimental finding regarding the similarities between the methanol- and ethanol-containing systems through the electrical properties (*vide post*). The propanol- and water-containing complexes are preferred by −5.0 kJ mol^{-1} and −22.2 kJ mol^{-1}. The preference towards the water-containing complex can be explained by the newly formed additional hydrogen bond between water and the nitrogen atom of the ligand (Fig. 3A). This cannot be formed in the case of the alcohols, due to the lack of additional hydrogen. It was also investigated what happens when starting from the methanol complex ($[Mo_2O_4(L)(MeOH)_2]\cdot 2MeOH$) and replacing one MeOH molecule with water, ethanol, or propanol. Since there are two types of methanol: directly Mo coordinated and (indirectly) crystallised one, two types of replacement can be carried out. By analysing the energetic properties, it was found that the relative Gibbs free energy of the reactions replacing one molecule is lower in the case of propanol (∼−1.8 kJ mol^{-1} in both cases) compared to ethanol (−1.3 and −1.0 kJ mol^{-1} for the directly and indirectly bonded cases, respectively). Furthermore, there is no significant difference between the direct or indirect cases in terms of energetics, ΔG = 0.3 kJ mol^{-1} for ethanol and 0.1 kJ mol^{-1} for propanol. However, in the case of water, the direct scenario is associated with −2.9 kJ mol^{-1} Gibbs free energy of the reaction, while the indirect case is −12.2 kJ mol^{-1}. The latter is due to an additional hydrogen bond formed between indirectly associated water and nitrogen of the ligand.

The observed trends in distances, hydrogen bonding interactions, and relative Gibbs free energies suggest that methanol and ethanol provide a similar coordination environment, while propanol induces slight deviations, and water leads to more pronounced structural rearrangements.

Electrical properties of molybdenum(VI) complexes

The study utilizing solid-state impedance spectroscopy (ss-IS) was used to investigate the electrical properties of two Mo-based complexes synthesized from MeOH/EtOH as the solvents. MeOH-based synthesis resulted in the formation of a complex, $[Mo_2O_4(L)(MeOH)_2]\cdot 2MeOH$ (**1***), which undergoes conversion to a complex, $[Mo_2O_4(L)(MeOH)_2]\cdot 2H_2O$ (**1**), upon exposure to air. In contrast, the EtOH-based synthesis, yielded a complex, $[Mo_2O_4(L)]_n$ (**2**). Thermal analysis showed that both complexes, $[Mo_2O_4(L)(MeOH)_2]\cdot 2H_2O$ (**1**) and $[Mo_2O_4(L)]_n$ (**2**), remained thermally stable up to approximately 350 °C, after the removal of the solvent molecules above 120 °C (from complex **1**). IS measurements were conducted between 30 and 200 °C to elucidate the conductivity behaviour of the compounds under thermal cycling conditions, which span a broad frequency spectrum, providing insights into their semiconducting nature.

The conductivity spectra of the complex, $[Mo_2O_4(L)]_n$ (**2**), presented in Fig. 4(b), exhibit two distinct regions during the heating and cooling cycles. The first region shows a frequency-dependent dispersion, which is more pronounced at lower temperatures and shifts beyond the measurable frequency range as the temperature increases. Consequently, the second region, defined by frequency-independent DC conductivity, becomes dominant at higher temperatures. The transition between these regions shifts to higher frequencies as the temperature increases, a phenomenon well-documented in the literature for both amorphous and crystalline semiconducting materials.[47–50] The frequency-independent DC plateau reflects the intrinsic electrical conductivity of the material, and its extent varies depending on the sample and temperature. The complex $[Mo_2O_4(L)]_n$ (**2**) showed thermal stability and exhibited no significant changes in conductivity during the heating and cooling runs, which is consistent with the absence of coordinated solvent molecules that could be lost upon heating, as noted in our previous investigations.[29–31] The DC conductivity of the complex $[Mo_2O_4(L)]_n$ (**2**) at 200 °C was 4.27 × 10^{-8} Ω^{-1} cm^{-1}. For the complex $[Mo_2O_4(L)(MeOH)_2]\cdot 2H_2O$ (**1**), significant differences in the conductivity spectra were observed between the heating and cooling cycles (SI, Fig. S16). During the heating cycle, a marked increase in conductivity was observed beyond 120 °C, correlating with the thermogravimetric (TG) analysis. This feature aligns well with the/structural transformation into the polynuclear form, $[Mo_2O_4(L)]_n$ (**2**), as confirmed by IR spectroscopy after heating to 200 °C. In the 40–120 °C range, the conductivity remained relatively constant, but increased significantly above 120 °C, implying the onset of structural changes. In the cooling run, the transformed complex exhibited a steady, monotonic

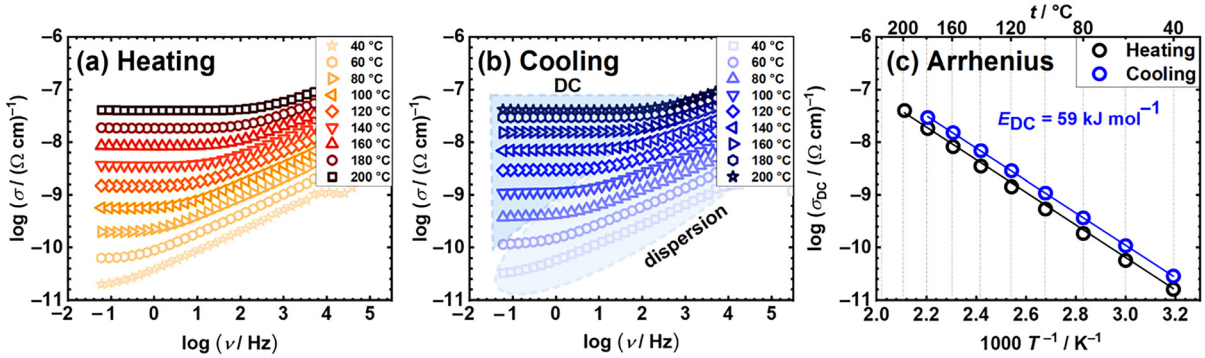

Fig. 4 Conductivity spectra of the polynuclear $[Mo_2O_4(L)]_n$ (**2**) compound in (a) heating and (b) cooling runs, along with the (c) Arrhenius plot for DC conductivity for both runs (black circle – heating and blue circle – cooling).

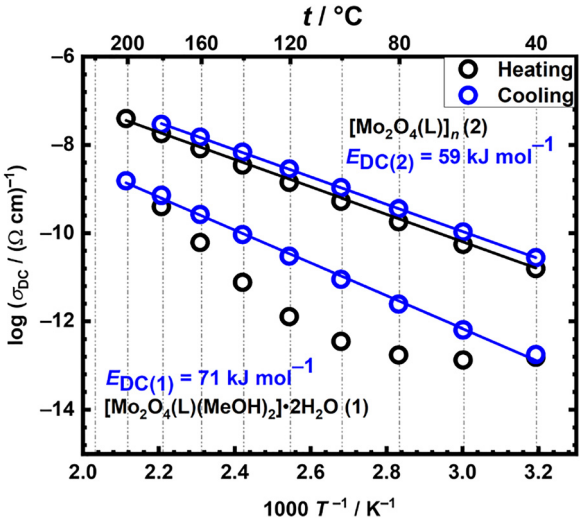

Fig. 5 Arrhenius plots for DC conductivity in both runs for the complex $[Mo_2O_4(L)(MeOH)_2]\cdot 2H_2O$ (**1**) and complex $[Mo_2O_4(L)]_n$ (**2**) (black circle – heating and blue circle – cooling).

Table 1 Activation energy and DC conductivity values of the complexes from this and previous investigation

Compounds	E_{DC}/kJ mol^{-1} [a]	σ/(Ω cm)$^{-1}$	Ref.
$[Mo_2O_4(L)(MeOH)_2]\cdot 2H_2O$	71	1.59×10^{-9} [b]	This study
$[Mo_2O_4(L)]_n$	59	4.27×10^{-8} [b]	
$[MoO_2(L^1)(MeOH)]$	65	1.82×10^{-9} [b]	29
$[MoO_2(L^1)]_n$	67	3.35×10^{-10} [b]	
$[MoO_2(L^2)(MeOH)]$	66	1.52×10^{-14} [b]	
$[MoO_2(L^2)(H_2O)]$	105	3.43×10^{-13} [b]	
$[MoO_2(L^3)(H_2O)]$	60	1.72×10^{-11} [b]	30
$[MoO_2(L^3)]_n$	40	8.77×10^{-8} [b]	
$[MoO_2(L^4)(H_2O)]$	84	1.80×10^{-10} [b]	
$[MoO_2(L^4)(MeOH)]$	81	8.96×10^{-11} [b]	
$[MoO_2(L^4)]_n$	95	2.66×10^{-9} [b]	
$[(NCS)(H_2O)NiL^5Pb(DMF)Cl]$	—	2.35×10^{-6} [c]	51
$[Cu_2(BPY)_2(DSNDI)]$	—	4.65×10^{-12} [c]	52
Rb-CD-MOF	—	6.8×10^{-10} [d]	

[a] The activation energy in the cooling run. [b] The conductivity values for the compounds were measured at 200 °C. [c] The conductivity values for the compounds were measured at RT. [d] The conductivity values for the compounds were measured at 57 °C. The ligand structures are provided in the SI, Table S6.

decrease in conductivity, as indicated by the spectra, suggesting the stabilization of the post-transformation structures. The DC conductivity of the complex $[Mo_2O_4(L)(MeOH)_2]\cdot 2H_2O$ (**1**) heated at 200 °C was 1.59×10^{-9} Ω^{-1} cm^{-1}, which is lower than that of the complex $[Mo_2O_4(L)]_n$ (**2**) (4.27×10^{-8} Ω^{-1} cm^{-1}).

The Arrhenius plot (Fig. 5) provides additional insights into the DC conductivity differences between the heating and cooling runs. The heating run for the complex $[Mo_2O_4(L)(MeOH)_2]\cdot 2H_2O$ (**1**) revealed non-linear changes in conductivity, indicating structural modifications, whereas the cooling one exhibited a more consistent and monotonic trend.

The complex $[Mo_2O_4(L)]_n$ (**2**) displayed thermal stability across both heating and cooling cycles, demonstrating consistent and monotonic behaviour throughout. Both complexes demonstrated semiconductive behaviour, with their DC conductivities adhering to an Arrhenius-type relationship. The activation energy (E_{DC}) for DC conductivity was derived from the slope of log(σ_{DC}) *versus* 1000/T plot using the following equation:

$$\sigma_{DC} = \sigma_0^* \exp(-E_{DC}/k_B T), \quad (1)$$

where σ_{DC} is the DC conductivity, σ_0^* is a preexponential factor, E_{DC} is the activation energy, k_B is Boltzmann's constant, and T is the absolute temperature. The activation energy for the complex $[Mo_2O_4(L)(MeOH)_2]\cdot 2H_2O$ (**1**) is determined to be 71 kJ mol^{-1}. In contrast, for the complex $[Mo_2O_4(L)]_n$ (**2**), it is 59 kJ mol^{-1}. This observed difference is consistent with the higher DC conductivity of $[Mo_2O_4(L)]_n$ (**2**).

Comparison of reported complexes[29,30,51,52] (Table 1) showed that Mo-based complexes generally exhibit conductivities, ranging from 10^{-8} to 10^{-14} Ω^{-1} cm^{-1} at 200 °C, with activation energies ranging from 40 to 105 kJ mol^{-1}. These variations can be attributed to differences in molecular packing, ligand effects, and the electronic nature of the coordination environment.[53–55] In particular, $[MoO_2(L^3)]_n$[30] shows relatively high conductivity (8.77×10^{-8} Ω^{-1} cm^{-1}) and the lowest activation energy (40 kJ mol^{-1}) among the Mo-based complexes presented in Table 1. In contrast, $[MoO_2(L^2)(H_2O)]$[29] has the highest activation energy (105 kJ mol^{-1}) and one of the lowest conductivities (3.43×10^{-13} Ω^{-1} cm^{-1}), indicating significant limitations in charge transport. Beyond the Mo complexes, the Schiff base-containing complex $[(NCS)(H_2O)NiL^5Pb(DMF)Cl]$[51] exhibits a conductivity of 2.35×10^{-6} Ω^{-1} cm^{-1} at RT, suggesting that the presence of a Schiff base ligand, combined with the hetero-metal coordination environment (Ni^{2+} and Pb^{2+}), enhances charge transport, see Table 1. This may result from an increased orbital overlap or alternative conduction pathways.[56] From the MOF-type complexes, $[Cu_2(BPY)_2(DSNDI)]$[52] shows a conductivity of 4.65×10^{-12} Ω^{-1} cm^{-1} at RT, while the Rb-CD-MOF[52] exhibits a conductivity of 6.8×10^{-10} Ω^{-1} cm^{-1} at 57 °C, see Table 1. This is consistent with the intrinsic porosity and reduced charge carrier density often associated with MOFs, which generally limit their electronic conductivity unless conductive linkers or dopants are introduced.[52,57]

In this study, the complex $[Mo_2O_4(L)]_n$ (**2**) exhibits the highest DC conductivity among Mo-based complexes, while also having the second-lowest activation energy, as presented in Table 1. This could be related to enhanced charge transport, likely owing to its polynuclear structure, which facilitates electron delocalisation, as described in the literature.[55,58] Relative to the other molybdenum complex in Table 1, the complex $[Mo_2O_4(L)(MeOH)_2]\cdot 2H_2O$ (**1**) shows a significantly higher conductivity by several orders of magnitude. A comparison of Mo-based complexes (Table 1) reveals that the $\{Mo_2O_4\}^{4+}$ core, featuring two metal centres, facilitates more efficient charge transport than the $\{MoO_2\}^{2+}$-based structures. The $\{Mo_2O_4\}^{4+}$ complexes include a ligand with two benzene rings that can act as bridging agents. The ligand with multiple benzene rings can promote electron transfer between the metal centres, contributing to the complex's conductivity.[59,60] The transformation of

the complex $[Mo_2O_4(L)(MeOH)_2]\cdot 2H_2O$ (**1**) into the $[Mo_2O_4(L)]_n$ (**2**) under heating significantly affects the conductivity, and the loss of coordinated solvents plays a crucial role. The lower activation energy of complex (**2**) indicates enhanced charge carrier mobility, likely due to its more stable, solvent-free structure.

Sensor properties of the dinuclear complex

The sensing properties of materials toward (gas) alcohol vapours have been extensively explored,[61–66] with a significant focus on metal oxides, polymers, MOFs, and various two-dimensional (2D) materials. However, the potential of coordination complexes as sensors for VOCs remains largely unexplored. In the case of MOS, semiconductors are classified into two primary types: n-type and p-type. The n-type is created by doping an intrinsic semiconductor with pentavalent elements, introducing additional free electrons that act as the majority charge carriers.[66–68] Conversely, the p-type semiconductor is formed by incorporating trivalent dopants, which generate holes as the predominant charge carriers.[63,64] Most MOS-based sensors exhibit an increase in resistance (*i.e.*, a decrease in conductivity) when exposed to alcohol vapours. In contrast, MOFs demonstrate opposite behaviour, showing a decrease in resistance and a corresponding increase in conductivity upon exposure.[61,62] When exposed to H_2O vapour, conductivity increases, but the mechanism differs from that of alcohols.[69,70]

The gas-sensing mechanism of MOS and MOF sensors is primarily governed by surface-controlled processes, where interactions between the sensor surface and adsorbed oxygen species influence resistance.[61,68,71] Oxygen molecules adsorb onto the semiconductor surface (depending on factors like temperature, particle size, surface area, and additives in the sensor material[66–75]), abstracting free electrons and decreasing electrical conductivity. This process involves the formation of various oxygen species, such as O_2^-(ads), O^{2-} (ads), and O^-(ads). At temperatures below 150 °C, O_2^- dominates, while at higher temperatures O^- is predominant.[71,75] The formation of ionosorbed oxygen creates an electron-depletion layer, increasing resistance by transferring electrons from the conduction band to the adsorbed oxygen. When alcohol vapours interact with these oxygen species, oxidation occurs, releasing electrons back into the semiconductor and increasing conductivity. This process enables the detection of alcohol vapours through measurable changes in resistance.[71,75] In contrast, H_2O does not contribute additional free electrons and instead facilitates proton transport through hydrogen bonding. The proton conductivity of metal–organic compounds relies on humidity, as H_2O molecules form extensive H-bond networks that enhance proton mobility.[69,70] More information about both the mechanisms and the following mathematical equations can be found in the SI.

In addition to conductivity, other critical parameters for assessing sensor performance include response and recovery time.[76] The response time (t_{res}) is defined as the duration required for the sensor to reach 90% of its total response, providing insight into the detection speed of the analyte gas. Conversely, the recovery time (t_{rec}) is the time required for the sensor to return to 90% of its original value in the absence of analyte gas.

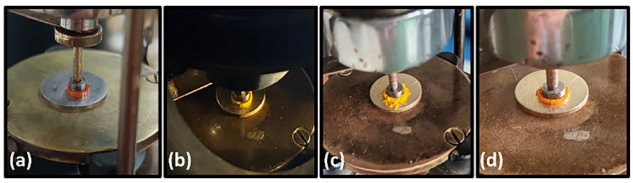

Fig. 6 Change in the colour of the dinuclear complex $[Mo_2O_4(L)(MeOH)_2]\cdot 2H_2O$ (**1**) after exposure to alcohol vapours. (a) Sample before exposure to any alcohol vapours and exposure to (b) MeOH vapours, (c) EtOH vapours and (d) PrOH vapours.

In this study, the complex $[Mo_2O_4(L)(MeOH)_2]\cdot 2H_2O$ (**1**) exhibited a distinct colour change upon exposure to alcohol vapours (Fig. 6 and SI, Fig. S14)—yellow with MeOH, light orange with EtOH, and intense orange with PrOH.

Such features suggest that the complex $[Mo_2O_4(L)(MeOH)_2]\cdot 2H_2O$ (**1**) could function as an effective gas sensor, especially for MeOH detection due to its reversible transformation. To further explore this potential, we employed ss-IS to measure the conductivity of the complex $[Mo_2O_4(L)(MeOH)_2]\cdot 2H_2O$ (**1**) under *in situ* exposure to MeOH, EtOH, PrOH and H_2O vapours. Building on the synthetic procedure and the observed solid-state structural transformation, we applied the same approach to evaluate the sensing properties. Consequently, the initial vapour concentrations for starting sensing testing were not quantified, and the study focused solely on the qualitative sensing behaviour. The sample was exposed to the corresponding vapours for several hours, which represented the maximum response capacity under the given conditions.

Conductivity measurements were conducted at RT in an isofrequency setup (at 1 Hz) over a defined period. Reversibility, reproducibility, and stability were assessed through exposure and relaxation cycles, supporting the potential of the complex as a selective vapour sensor. The results are summarised in Table 2 and Fig. 7. An increase in conductivity was observed across all vapours. The primary focus was on alcohol vapours, with H_2O serving as a reference system. MeOH and EtOH induced a rapid initial increase in the conductivity, whereas PrOH exhibited a slower response during the 1st exposure cycle. However, in the 2nd cycle, all alcohol vapours generated an immediate conductivity change. In contrast, H_2O consistently demonstrated a slow response in both cycles. Following vapour exposure, the samples were allowed to recover at RT and under standard atmospheric conditions. Notably, MeOH did not fully return to its original pre-exposure conductivity after 1st cycle.

This incomplete recovery, as discussed in the paragraph Crystal and molecular structure and shown in Fig. S15(c), may be attributed to structural changes, where the crystal H_2O molecules are replaced by MeOH upon vapour exposure and subsequently revert to H_2O molecules during relaxation. However, not all sites may undergo complete exchange back to their original composition, leaving residual MeOH molecules. In the

Table 2 Conductivity and response time after exposure of the complex $[Mo_2O_4(L)(MeOH)_2]\cdot 2H_2O$ (**1**) to H_2O, MeOH, EtOH and PrOH vapours in for 1st and 2nd cycles

	σ (Ω cm)$^{-1}$		$\Delta\sigma$ (Ω cm)$^{-1a}$		t_{res} (s)	
Vapours	1st cycle	2nd cycle	1st cycle	2nd cycle	1st cycle	2nd cycle
MeOH	6.73×10^{-7}	2.21×10^{-6}	1.02×10^{-6}	1.41×10^{-6}	490	130
EtOH	5.60×10^{-7}	8.85×10^{-8}	6.92×10^{-6}	5.75×10^{-5}	520	690
PrOH	2.52×10^{-8}	1.15×10^{-9}	3.63×10^{-5}	1.35×10^{-3}	12 410	1980
H_2O	3.85×10^{-10}	2.59×10^{-10}	3.09×10^{-3}	5.50×10^{-3}	14 640	1120

[a] Change in conductivity for both cycles is calculated as a difference in the conductivity value at the plateau and the beginning of the vapour exposure ($\Delta\sigma = \sigma_{plateau} - \sigma_{before}$).

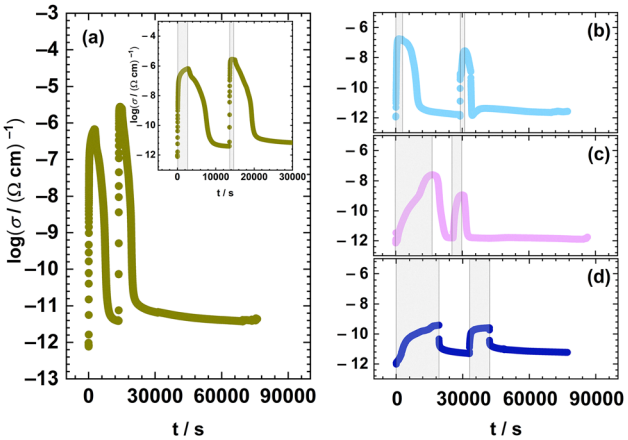

Fig. 7 Conductivity spectra of the $[Mo_2O_4(L)(MeOH)_2]\cdot 2H_2O$ (**1**) compound upon exposure to (a) MeOH (dark yellow circles), (b) EtOH (blue circles), (c) PrOH (pink circles) and (d) H_2O (dark blue circles) vapours. Measurements were conducted at 1 Hz.

2nd exposure cycle, MeOH exhibited full recovery of pre-exposure conductivity, suggesting that equilibrium was achieved. The slower initial response observed for PrOH may be due to the replacement of smaller H_2O molecules with larger PrOH ones. However, after the 1st exposure, the structural transition was no longer necessary, leading to a more rapid change in the 2nd cycle. This suggests that the material undergoes irreversible structural adaptation upon initial exposure to PrOH vapours, facilitating a faster response in the 2nd cycle.

The maximum conductivity value ($\sigma_{plateau}$) followed the trend: MeOH ~ EtOH ≫ PrOH > H_2O. Specifically, in 1st cycle exposure, MeOH exhibited the highest value (6.73×10^{-7} Ω^{-1} cm^{-1}), followed by EtOH (5.60×10^{-7} Ω^{-1}cm^{-1}, PrOH (2.52×10^{-8} Ω^{-1}cm^{-1}), and H_2O (at 3.85×10^{-10} Ω^{-1} cm^{-1}). Upon 2nd cycle exposure, MeOH demonstrated conductivity enhancement, increasing to 2.21×10^{-6} Ω^{-1} cm^{-1}. In contrast, EtOH, PrOH, and H_2O exhibited reverse behaviour, decreasing to 8.85×10^{-8} Ω^{-1} cm^{-1}, 1.15×10^{-9} Ω^{-1} cm^{-1}, and 1.75×10^{-10} Ω^{-1} cm^{-1}, respectively. A slightly smaller reduction is observed for PrOH, where conductivity decreased nearly an order of magnitude.

Remarkably, MeOH induced a conductivity change spanning six (6) orders of magnitude during the 1st cycle, a variation that persisted in the 2nd cycle, highlighting its significant influence on the electrical properties of the complex (**2**). The recovery time varied depending on the vapour type: MeOH and EtOH required longer recovery periods, whereas PrOH and H_2O returned to baseline conductivity more rapidly. MeOH exhibited a shorter t_{rec} than EtOH, whereas PrOH demonstrated the fastest recovery.

Literature studies have indicated that t_{res} and t_{rec} are significantly influenced by the optimal working temperature.[67,71] Most reported sensors operate at elevated temperatures, typically between 150 and 300 °C, where t_{res} and t_{rec} are significantly reduced to the order of seconds. However, the primary challenge in high-temperature operation is the requirement for an external heating setup, which limits its practical applications. The development of sensors that are capable of efficient operation at RT remains a critical goal in the field. M. Aleksanyan *et al.*[71] investigated ZnO nanostructured films for EtOH vapour sensing at various temperatures. Their findings showed that at 100 °C, t_{res} was of the order of 10^3 s, whereas increasing the temperature to 300 °C reduced the t_{res} to 12 s. While K. Phasuksom *et al.*[77] reported that t_{res} for MeOH at RT was approximately 15 minutes for polyindole.

In this study, the complex $[Mo_2O_4(L)(MeOH)_2]\cdot 2H_2O$ (**1**) was evaluated at RT for alcohol and H_2O vapour sensing over two consecutive cycles (Fig. 8 and SI, Fig. S17). The sensor

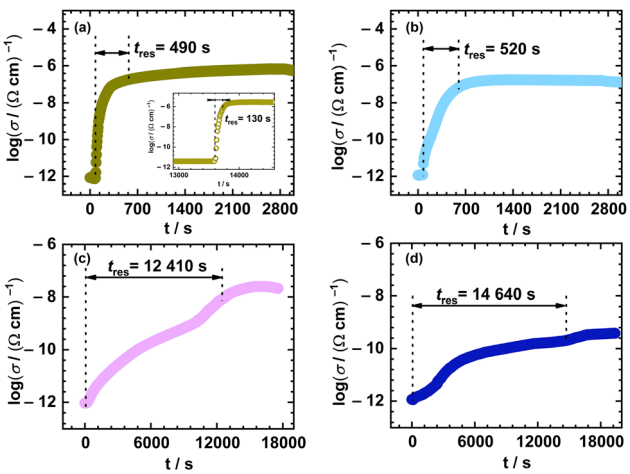

Fig. 8 Conductivity spectra of the $[Mo_2O_4(L)(MeOH)_2]\cdot 2H_2O$ (**1**) compound in the 1st cycle. Exposure to (a) MeOH (dark yellow circles – 1st cycle, inset – 2nd cycle), (b) EtOH (blue circles), (c) PrOH (pink circles) and (d) H_2O (dark blue circles) vapours.

demonstrated distinct response behaviour based on the analyte, indicating its potential for selective use. Notably, in the 1st cycle, PrOH and H_2O display step-like conductivity increases, unlike the sharp and rapid responses of MeOH and EtOH, following a fundamentally different sensing mechanism. K. Mukherjee *et al.*[78] proposed that the mechanism involving PrOH may proceed in multiple steps before it is ultimately converted to carbon dioxide and water. This multi-step process could explain why the conductivity response to PrOH vapour in our study shows two distinct ''steps'' before reaching a plateau, indicating complex interactions and reaction pathways occurring during sensor exposure to PrOH vapours. It seems that this behavior results from steric hindrance and slower diffusion to coordination sites. Furthermore, it suggests that the response to PrOH is not a simple, one-step process, but rather a series of intermediate steps that contribute to the final sensor response. On the other hand, for H_2O, the mechanism is fundamentally different. Water interacts *via* hydrogen bonding, and its conductivity arises from charge transport along hydrogen-bonded networks. MeOH demonstrated the best performance, with a t_{res} of 490 s, followed closely by EtOH at 520 s. The response times of PrOH and H_2O were slightly higher at RT than those of MeOH and EtOH during the 1st cycle.

After this initial transformation, the complexes stabilize, and no further structural changes or solvent exchange occur in subsequent cycles. In the 2nd cycle, following the relaxation period during which the conductivity returned to its pre-exposure value, MeOH showed the most significant enhancement, reducing its t_{res} to 130 s while maintaining a single-step response. Both PrOH and H_2O exhibit smoother but still slower responses. As expected, the structural transformation/solvent exchange has already occurred, sensing proceeds *via* surface-level interactions: physisorption affecting charge transport in alcohols, and proton conductivity *via* the H-bond network in H_2O. These surface-controlled processes remain consistent and fully reversible, enabling reliable two-cycle sensing performance. Interestingly, EtOH exhibited hybrid behaviour, combining the rapid initial response of MeOH with a gradual rise toward a plateau, similar to that of PrOH.

Greatly, the t_{res} values for PrOH and H_2O were reduced by an order of magnitude in the 2nd cycle, reaching 1980 s and 1120 s, respectively. The reduction in t_{res} can be attributed to a structural transition within the complex, likely driven by an exchange between the coordinated water and alcohol molecules.

Despite the lack of further structural or solvent exchange in later cycles, all complexes remain sensing-active. The conductivity response arises from reversible surface physisorption and hydrogen bonding, which affect charge transport without altering the coordination environment. This dynamic rearrangement facilitates a more efficient interaction with vapour-phase analytes upon subsequent exposure, enabling faster detection. These research findings highlight the exceptional sensing performance of $[Mo_2O_4(L)(MeOH)_2]\cdot 2H_2O$ (**1**), particularly for MeOH detection.

The ability to detect MeOH at RT without external activation highlights the low-power potential of this system. As mentioned, previous studies have demonstrated RT MeOH sensing using nanostructured metal oxides and hybrid composites.[71,77] Also, it is important to note that the current system shows selective and reversible RT sensing of multiple alcohols based on distinct conduction mechanisms. More broadly, the development of RT-operable sensors is a key goal for portable and energy-efficient devices. High-performance RT sensors have recently been demonstrated for inorganic gases such as NO_2 and NH_3 using heterostructured CdS nanowires and high-entropy sulfides,[79,80] highlighting the technological push in this direction. Our findings extend this paradigm to organic vapours, offering the possibility of stable RT sensing performance without additional activation.

The change in conductivity ($\Delta\sigma$) for both cycles is calculated as the difference in the conductivity value at the plateau and the beginning of the vapour exposure ($\Delta\sigma = \sigma_{plateau} - \sigma_{before}$), see Fig. 9 and Table 2. This illustrates the dynamic interaction between the sensor complex and tested vapours, revealing their sensitivity and adaptability over repeated exposure cycles. In the 1st cycle, MeOH induces the most significant increase in conductivity, rising by approximately six orders of magnitude, followed by EtOH, PrOH, and H_2O. This trend is governed by molecular properties such as polarity, adsorption kinetics, and charge transfer dynamics, which influence the degree of interaction between each vapour and the sensor's active sites.[81,82]

The strong response to MeOH suggests an elevated level of interaction, possibly due to its smaller molecular size and higher dipole moment, which facilitates efficient charge transfer.[83] MeOH exhibits the most stable response, with minimal changes in conductivity, whereas H_2O shows a similar effect but relies on proton conductivity rather than electronic charge transfer. The light adjustment across the conductivity may indicate an adaptation phase, resulting from surface reorganization, partial desorption of previously adsorbed molecules, or equilibrium being established between the sensor material and the vapour environment. These findings suggest

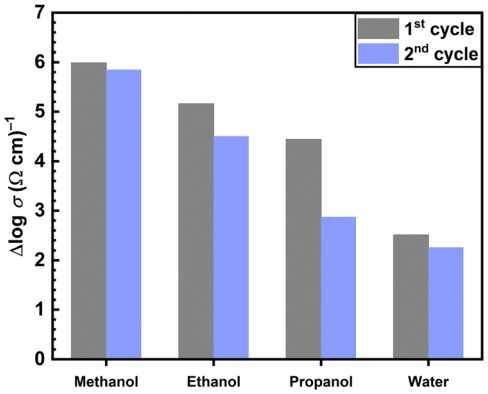

Fig. 9 Change in the conductivity of the dinuclear complex $[Mo_2O_4(L)(MeOH)_2]\cdot 2H_2O$ (**1**) for 1st and 2nd cycles. The change in the conductivity of both cycles is calculated as the difference between the conductivity values at the plateau and the beginning of vapour exposure ($\Delta\sigma = \sigma_{plateau} - \sigma_{before}$).

that the sensor reaches a more stable operational state over repeated exposures, enhancing its reliability.

As presented in the SI section, the alcohol-sensing mechanism involves the release of electrons back to the surface of the sensing material, leading to an increase in conductivity. Based on this mechanism, one would expect PrOH to exhibit the highest response, with MeOH showing the lowest due to electron release being the primary factor influencing conductivity. However, the experimental results in this study do not fully align with this prediction, suggesting that other factors also contribute to the sensor behaviour. In particular, the surface area available for interaction with the target vapour appears to play a role in shaping the sensor properties. Given that MeOH molecules are smaller than EtOH and PrOH molecules, it is plausible that MeOH molecules may pack more densely on the surface layer of the semiconductor material than on larger PrOH molecules.

Solvent polarity also plays a significant role in determining the sensing properties of the materials. The interaction between the sensing element and the analyte can be significantly influenced by the polarity of the surrounding medium, affecting sensitivity, t_{res}, and detection limits.[84,85] The polarity values of common solvents[86] are presented Table 3, highlighting MeOH as the most polar alcohol (0.762) and PrOH as the least polar alcohol (0.617). H_2O, with a polarity value of 1.000, follows a different sensing mechanism. The high polarity of MeOH significantly enhances its interaction with polar sensing materials, leading to an improved sensing response. This is likely due to stronger dipole–dipole interactions and hydrogen bonding, which facilitate the adsorption of analyte molecules onto the sensing surface.

Additionally, structural analysis of the dinuclear complex $[Mo_2O_4(L)(MeOH)_2]\cdot 2H_2O$ (**1**) reveals that it forms 1D chains connected through hydrogen bonds involving MeOH molecules (Fig. S15 (d)). This hydrogen-bonding network enhances the overall sensing performance by promoting efficient analyte adsorption and transport. In contrast, PrOH, with the lowest polarity among the alcohols examined, demonstrates a weaker sensing response. The lower response may be influenced by polarity, and thus weaker intermolecular interactions with the sensing material. Moreover, due to the larger molecular size of EtOH and PrOH compared to MeOH, the structural organization of the dinuclear complex is altered, disrupting the 1D hydrogen-bonded network (see Fig. 3). This structural modification may further contribute to the lower sensing efficiency observed for larger alcohols, as the altered hydrogen-bonding pattern affects the analyte accessibility and adsorption onto the sensing interface.

Further rationalisation involved cyclic exposure experiments using methanol vapours, see Fig. 10. Methanol was selected as the representative analyte due to its pronounced effect on the material's conductivity. The experimental setup was additionally optimized to ensure system stability and reproducibility. The sensing chamber was saturated with methanol vapor by leaving it overnight, allowing the system to reach equilibrium.

Table 3 Polarity values for H_2O and alcohol vapours[86]

Solvent	Polarity
H_2O	1.000
MeOH	0.762
EtOH	0.654
PrOH	0.617

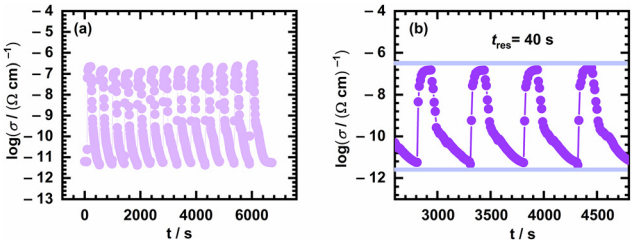

Fig. 10 Conductivity of $[Mo_2O_4(L)(MeOH)_2]\cdot 2H_2O$ (**1**) in cyclisation experiments upon MeOH exposure (a) 13 cycles and (b) inset: enlarged 4 cycles.

Upon exposure of the sample to methanol vapour, a clear increase in conductivity was observed. Subsequent cyclic introduction and removal of methanol vapour resulted in increase/decrease in conductivity. A total of additional 13 exposure–removal cycles were performed, as shown in Fig. 10. While response time was determined down to 40 seconds, the recovery time was 230 seconds. The sensor demonstrated excellent long-term stability, maintaining consistent repeated performance after 30 days from the initial measurements. The results obtained are promising and warrant further investigation, forming the basis for our continued research on Mo-based sensors.

Additional tests were performed with isopropanol (i-PrOH) and pentanol vapors. Exposure to i-PrOH resulted in an increase in conductivity by approximately two orders of magnitude, whereas no response was observed for pentanol. Testing with tert-butanol was not feasible due to experimental limitations and its low melting point under the ambient conditions. The observed selectivity can be attributed to the molecular size and vapor pressure effects—lower linear alcohols (methanol, ethanol, and propanol) more readily diffuse and interact with the sensing layer, while branched or longer-chain alcohols exhibit hindered adsorption and weaker charge transfer. Consequently, the material demonstrates sensitivity primarily toward lower aliphatic alcohols (C1–C3).

In this study, two novel Mo-based complexes were successfully synthesized. Both complex the $[Mo_2O_4(L)(MeOH)_2]\cdot 2H_2O$ (**1**) and complex $[Mo_2O_4(L)]_n$ (**2**) exhibited excellent conductivity at 200 °C, demonstrating their potential for application as semiconductors. Additionally, the complex $[Mo_2O_4(L)(MeOH)_2]\cdot 2H_2O$ (**1**) showed significant potential for use as a sensor for VOCs and H_2O detection.

Experimental

Materials

Ligand synthesis

Solution-based synthesis. The **H_4L** ligand was obtained by condensation of oxalyldihydrazide (0.5324 g, 4.5082 mmol,

SIGMA-ALDRICH) and salicylaldehyd (0.94 mL, 1.1008 g, 9.0164 mmol, Fluka AG) in molar ratio of 1 : 2, in MeOH (50 mL). A white powder product was obtained.

Mechanochemical synthesis. The same ligand can be obtained by mechanochemical synthesis. Oxalyldihydrazide (0.0200 g, 0.1694 mmol, SIGMA-ALDRICH) and salicylaldehyde (36.1 μL, 0.0414 g, 0.3387 mmol, Fluka AG) were put in the Teflon jar. 10 μL MeOH was added and milled for 30 min at 25 Hz. A white powder product was obtained.

H_4L. Colour: white and yield for solution-based synthesis: 85.32%

IR-ATR (cm^{-1}): 3279 and 3200 (O–H), 3144 (C–H), 3000 (C–H), 1664 (C = O), and 1602 (C = N)

DSC: T_e = 308.17 °C, E = 64.55 kJ mol^{-1}

Molybdenum(VI) complexes

Dinuclear complex. In a 100 mL round bottom flask, the ligand **H_4L** (0.0477 g, 0.1402 mmol) was added to the MeOH (30 mL) with stirring. After one hour, $[MoO_2(acac)_2]$ (0.0914 g, 0.2804 mmol) was added. The suspension was refluxed for seven hours and left at RT. The product was filtered off and dried. Yellow crystals were obtained. After exposure to air, the dinuclear complex turned orange. If the reaction was performed *in situ* with oxalyldihydrazide (0.0200 g, 0.1693 mmol), salicylaldehyde (0.0414 g, 0.3387 mmol) and $[MoO_2(acac)_2]$ (0.1105 g, 0.3387 mmol) for five hours, the same product was formed.

$[Mo_2O_4(L)(MeOH)_2]\cdot 2H_2O$ (1). Colour: orange and yield: 47.91%

IR-ATR (cm^{-1}): 3371 (OH), 1646 (H_2O), 1599 (C═N), 1535 (C═C), 1256 (C–O), 1033 (MeOH), 898 and 868 (Mo═O)

TGA: $(MeOH \text{ and } H_2O)_{theo}$: 7.38%, $(MeOH \text{ and } H_2O)_{exp}$: 7.73%, MoO_{3theo}: 21.22%, and MoO_{3exp}: 19.47%

Polynuclear complex. In a 100 mL round bottom flask, the ligand **H_4L** (0.0487 g, 0.1430 mmol) was added to EtOH, acetonitrile or acetone (30 mL) with stirring. After one hour, $[MoO_2(acac)_2]$ (0.0933 g, 0.2860 mmol) was added. The suspension was refluxed for seven hours and left at RT. The product was filtered off and dried.

If the dinuclear complex $[Mo_2O_4(L)(MeOH)_2]\cdot 2H_2O$ (**1**) was heated to 145 °C, it transformed to the polynuclear complex $[Mo_2O_4(L)]_n$ (**2**). When the complex was exposed to water or alcohol vapours, it did not convert back to the dinuclear complex.

$[Mo_2O_4(L)]_n$ (2). Colour: brown and yield: 55.11%

IR-ATR (cm^{-1}): 1595 (C═N), 1522 (C═C), 1222 (C–O), and 836 and 810 (Mo═O)

TGA: MoO_{3theo}: 24.90% and MoO_{3exp}: 23.67%

Transformation of the dinuclear complex in the solid state $[Mo_2O_4(L)(MeOH)_2]\cdot 2H_2O$ (1). A small amount of the dinuclear complex $[Mo_2O_4(L)(MeOH)_2]\cdot 2H_2O$ (**1**) was placed in a 5 mL beaker, which was then positioned inside a 10 mL glass beaker containing the desired alcohol (MeOH, EtOH, and PrOH) or H_2O vapor at a concentration of 100 ppm. The system was sealed with parafilm to ensure controlled exposure of the complex to the vapours. Vapour concentrations were calculated using eqn (2):[87,88]

$$C_{ppm} = \frac{V_{\mu L} D_{g\,mL^{-1}}}{M_{g\,mol^{-1}} V_{mL}} \times 2.46 \times 10^7 \quad (2)$$

where C_{ppm} is the required gas concentration, $D_{g\,mL^{-1}}$ is the density of the liquid, $V_{\mu L}$ is the used solvent volume, V_{mL} is the volume of the dilutant air (equal to the volume of the test chamber) and $M_{g\,mol^{-1}}$ is the molecular weight of the solvent.

Methanol vapours. When exposed to MeOH vapours, the dinuclear complex $[Mo_2O_4(L)(MeOH)_2]\cdot 2H_2O$ (**1**) changes colour from orange to yellow. Once the complex is removed from MeOH vapours and back to air, it changes colour back to orange.

Ethanol vapours. When exposed to EtOH vapours, the dinuclear complex $[Mo_2O_4(L)(MeOH)_2]\cdot 2H_2O$ (**1**) changes colour from orange to light orange. Once the complex is removed from EtOH vapours and back to air it remains the same.

Propanol vapours. When exposed to PrOH vapours, the dinuclear complex $[Mo_2O_4(L)(MeOH)_2]\cdot 2H_2O$ (**1**) changes colour from orange to intense orange. Once the complex is removed from PrOH vapours and back to the air it does not change.

Water vapours. When exposed to H_2O vapours, the dinuclear complex $[Mo_2O_4(L)(MeOH)_2]\cdot 2H_2O$ (**1**)remains in the same orange colour.

Methods

The prepared compounds were characterized by infrared spectroscopy (IR-ATR, Infrared spectroscopy-Attenuated Total Reflectance), thermogravimetric analysis (TGA), differential scanning calorimetry (DSC), single crystal X-ray diffraction (SCXRD), and solid-state impedance spectroscopy (ss-IS).

IR-ATR analysis was performed using a PerkinElmer Spectrum Two spectrometer equipped with a diamond ATR attachment. The measurement was carried out in the 4000–400 cm^{-1} range with four scans. The spectra were processed and analysed with Origin program version 2020.

A Mettler–Toledo TGA/DSC 3+ instrument was used for differential scanning calorimetry (DSC) analysis in the range of 25–400 °C in an inert N_2 atmosphere with a 50 mL min^{-1} flow rate and the heating of 10 °C min^{-1}. The samples were measured in opened Al_2O_3 crucibles. The obtained data were processed with the Mettler STARe Evaluation Software v18.00 and Origin program version 2020.

Thermogravimetric (TGA) analysis was performed using Mettler–Toledo TGA/DSC 3+ in closed Al_2O_3 crucibles. All experiments were performed in an O_2 atmosphere with a flow rate of 200 cm^3 min^{-1} and heating rate at 10 °C min^{-1}. The measurements were carried out in the wide temperature range 25 °C–600 °C. The results were processed with Mettler STARe Evaluation Software v18.00 and Origin program version 2020.

Semiconductor properties using ss-IS. The complex impedance was measured across a wide range of temperatures (30–200 °C, in 10 °C increments) and a frequency range (0.01 Hz–1 MHz) utilizing a Novocontrol Alpha–AN spectrometer. Temperature was held within ±0.2 °C. For IS measurements, cylindrical

disks (diameter:5 mm; thickness: 1 mm) were obtained from powder samples using hydraulic press under a uniform load of 2×10^3 kg. On both disk sides, gold electrodes (3.8 mm) for electrical contact were sputtered using a Quorum Technologies SC7620 magnetron. The sample was positioned in the ''sandwich'' configuration in the BDS cell. The measurement results were processed with Origin program version 2020.

Exposure to water and alcohol vapours using ss-IS. The complex impedance of the samples was measured at room temperature in isofrequency mode (1 Hz) using a Novocontrol Alpha–AN broadband dielectric spectrometer. Measurements were performed on prepared disk-shaped samples placed in a BDS cell within a home-made multifunctional environmental chamber specifically constructed for electrical measurements. Vapours (water and various alcohols) were introduced by adding the respective liquids into a 60 mL glass beaker inside the sealed chamber, allowing the sample to be exposed to the corresponding vapours for several hours. No external vapour delivery system or gas flow was employed.

Based on the best obtained results, additional cyclization experiments were carried out using methanol vapors. To ensure sufficient vapor saturation, the reaction chamber was pre-saturated with methanol overnight prior to initiating the experiment. The humidity inside the chamber was monitored using a hygrometer, confirming that a saturated atmosphere with a relative humidity of approximately 100% was maintained. During the cycling procedure, after exposure to fully saturated water or alcohol vapors, the sample was removed from the chamber and allowed to equilibrate under ambient laboratory conditions (22 °C, air-conditioned). Through this relaxation stage, equilibrium with the ambient RH was spontaneously established as the humidity decreased freely (''free fall'') until the ambient RH was reached. After a certain period, the sample was reintroduced into the chamber saturated with the corresponding vapors under fully saturated conditions. Data acquisition and analysis were conducted using the Origin software package (version 2020).

Crystallography

The single crystal of $[Mo_2O_4(L)(MeOH)_2]\cdot 2MeOH$ (**1***) of appropriate quality was selected for diffraction experiments. Data were recorded using a Rigaku XtaLAB Synergy-S diffractometer equipped with a Dualflex source (Cu Kα radiation, λ= 1.54184 Å) and a HyPix detector. Data were gathered *via* ω-scans at 170 K and processed with the CrysAlis program package.[89]

A summary of general crystallographic data is presented in Table S1 (SI). The structures were solved by dual-space methods with SHELXT.[90] The refinement was done *via* a full-matrix least-squares method based on F^2 values against all reflections, including anisotropic displacement parameters for all non-H atoms. Hydrogen atoms attached to carbon atoms were placed in geometrically idealized positions and refined by using riding model, with $U_{iso} = 1.2U_{eq}$ of the connected carbon atom, or as ideal CH_3 groups, with $U_{iso} = 1.5U_{eq}$. Hydrogen atoms attached to heteroatoms were located in different Fourier maps in final stages of the refinement procedure. All refinements were conducted using SHELXL.[91] The SHELX programs were operated within the Olex2 suite.[92] Geometrical calculations were performed by Platon[93] and molecular graphics were produced using Mercury.[94] The structure of $[Mo_2O_4(L)(MeOH)_2]\cdot 2MeOH$ (**1***) was solved as a two-component non-merohedral twin, with three twin domains present in a ratio of 0.217 : 0.066 : 0.717. CCDC 2434680 contains supplementary crystallographic data for this paper.

Molecular modelling methods

To compare the structures and stabilities of the different molybdenum complexes, the crystal structure of $[Mo_2O_4(L)(MeOH)_2]\cdot 2MeOH$ (**1***) was used as the starting point. The structural information from the crystal structure was used to prepare an input file for density functional theory calculations. The Becke Three-Parameter Hybrid Functional (B3LYP)[95] as it is implemented in the Gaussian 16 program package[96] was employed during optimization in combination with SDD effective core potential[97–99] for molybdenum and the 6-31G(d,p) basis set for nonmetal atoms and optimizations and frequency calculations were carried out. To fine tune the accuracy, Grimme's dispersion correction with the D3 damping function[100] was added by using the empirical dispersion = GD3 keyword. Starting from the optimized $[Mo_2O_4(L)(MeOH)_2]\cdot 2MeOH$ (**1***) geometry, methanol molecules were replaced by 1–4 water, ethanol or propanol, accordingly. Thereafter, each new corresponding complex was re-optimized and frequency calculations were carried out at the same level of theory described above. The structural and thermodynamic properties of the complexes were compared and analysed.

Conclusions

VOC detection plays a vital role in various sectors, requiring advanced, sensitive, and reliable sensors that integrate engineering and chemistry for effective device development and material design.

The findings of this study underscore the potential of coordination complexes as effective semiconductors and sensors for alcohol and H_2O vapours. Complex $[Mo_2O_4(L)]_n$ (**2**) exhibited good electrical properties, with a high conductivity of $4.27 \times 10^{-8}\ \Omega^{-1}\ cm^{-1}$ at 200 °C and a low activation energy of 59 kJ mol^{-1}, reinforcing its suitability for semiconductor applications. Similarly, complex $[Mo_2O_4(L)(MeOH)_2]\cdot 2H_2O$ (**1**) demonstrated a notable conductivity of $1.59 \times 10^{-9}\ \Omega^{-1}\ cm^{-1}$ at 200 °C. Computational calculations demonstrated that methanol provides the most stable and structurally consistent coordination environment among the studied solvents, as evidenced by its minimal deviation in Mo–O bond distances and strong hydrogen bonding interactions. The structural integrity of the methanol complex remains largely preserved, whereas other solvents induce greater distortions in the $[Mo_2O_4(L)]$ core. These findings suggest that methanol facilitates the most stable coordination geometry, minimizing structural perturbations within the complex.

Upon exposure to alcohol and water vapours, complex $[Mo_2O_4(L)(MeOH)_2]\cdot 2H_2O$ (**1**) exhibited a significant conductivity increase, indicating strong interactions and efficient charge transport. Specifically, exposure to MeOH led to a six-order magnitude increase in conductivity, highlighting its high sensitivity. Furthermore, the t_{res} value for MeOH detection was 130 s, making it a highly effective sensor at RT. Likewise, exposure to EtOH resulted in a five-order magnitude increase, while PrOH led to a four-and-a-half-order magnitude increase in conductivity. Additionally, the observed colour change upon exposure provides a convenient visual detection feature, further enhancing its practical applications. Distinct response trends between the 1st and 2nd vapor exposure cycles suggest that the sensing mechanism evolves from an initial structural transformation and coordination-driven process to a reversible surface-level sensing mode governed by kinetic adsorption and hydrogen bonding. The optimized experimental configuration exhibited consistent and reproducible sensor responses upon exposure to methanol vapor. The repeatability observed across 15 cycles reinforces the suitability of Mo-based coordination complexes as promising candidates for vapor-phase sensing applications. The system demonstrated a response time of 40 s, while the recovery time was 230 s. These results are particularly significant given the limited number of coordination complexes reported in the literature that can function as VOC sensors at RT. The stability and reliability of complex $[Mo_2O_4(L)(MeOH)_2]\cdot 2H_2O$ (**1**), along with the excellent conductivity of complex $[Mo_2O_4(L)]_n$ (**2**), and the ability to operate at RT without external activation, position these coordination complexes as promising candidates for advanced low-power sensing applications and semiconductors. These findings underline the novelty of this system based on molybdenum coordination complexes, which enables selective RT sensing of organic vapors through a combined structural and surface-sensing mechanism.

Building upon these findings, future research will focus on the synthesis of novel coordination complexes incorporating two metal centres with similar properties. This approach aims to develop highly efficient sensors for the selective detection of various VOCs at RT, expanding the potential applications of coordination complexes.

Author contributions

Conceptualization: L. P. and J. P. Data curation: J. S., M. R., B. F., L. P., and J. P. Formal analysis: J. S., M. R., and B. F. Funding acquisition: L. P. and J. P. Investigation: J. S., M. R., B. F., L. P., and J. P. Methodology: B. F., L. P., and J. P. Project administration: L. P. and J. P. Resources: B. F., L. P., and J. P. Software: J. S., M. R., B. F., L. P., and J. P. Supervision: L. P. and J. P. Validation: J. S., M. R., and B. F. Visualization: J. S., M. R., and B. F. Writing – original draft: J. S., L. P., and J. P. Writing – review and editing: J. S., M. R., B. F., L. P., and J. P.

Conflicts of interest

There are no conflicts to declare.

Data availability

The data supporting this article have been included as part of the supplementary information (SI). Supplementary information includes IR-ATR for ligand and complexes, DSC for the ligand, TGA analysis for the complexes, crystallographic data for $[Mo_2O_4(L)(MeOH)_2]\cdot 2MeOH$, Optimised data for the structures, Conductivity spectra for $[Mo_2O_4(L)(MeOH)_2]\cdot 2H_2O$ and Gas sensing mechanism discussion. See DOI: https://doi.org/10.1039/d5tc03013g.

CCDC 2434680 contain the supplementary crystallographic data for this paper.[101]

Acknowledgements

J. S. and J. P. acknowledge the support of project CIuK (grant KK.01.1.1.02.0016) co-financed by the Croatian Government and the European Union through the European Regional Development Fund-Competitiveness and Cohesion Operational Programme. J. S. acknowledges Edi Topić and Dino Kuzman for their help and valuable advice with the crystallographic data. This work was also supported by the internal RBI funding scheme ZI-2023 program (ZI5-25) through National Recovery and Resilience Plan 2021-2026 (NPOO), funded by the European Union's NextGenerationEU program. The GITDA (Governmental Information-Technology Development Agency, Hungary) is gratefully acknowledged for allocating computing resources used in this work. Calculations have also been carried out using resources provided by Wroclaw Centre for Networking and Supercomputing (https://wcss.pl).

References

1 D. Kohl, *J. Phys. D: Appl. Phys.*, 2001, **34**, R125–R149.
2 X. Liu, S. Cheng, H. Liu, S. Hu, D. Zhang and H. A. Ning, *Sensors*, 2012, **12**, 9635–9665.
3 T.-V. Dinh, I.-Y. Choi, Y.-S. Son and J.-C. Kim, *Sens. Actuators, B*, 2016, **231**, 529–538.
4 C. Di Natale, A. Macagnano, E. Martinelli, R. Paolesse, G. D'Arcangelo, C. Roscioni, A. Finazzi-Agró and A. D'Amico, *Biosens. Bioelectron.*, 2003, **18**, 1209–1218.
5 J. W. D. Grate, S. L. Rose-Pehrsson and D. L. Venezky, *Anal. Chem.*, 1993, **65**, 1868–1881.
6 B. Buszewski, A. Ulanowska, T. Ligor, N. Denderz and A. Amann, *Biomed. Chromatogr.*, 2009, **23**, 551–556.
7 N. A. Rakow and K. S. Suslick, *Nature*, 2000, **406**, 710–713.
8 S.-Y. Cho, H.-W. Yoo, J. Y. Kim, W.-B. Jung, M. L. Jin, J.-S. Kim, H.-J. Jeon and H.-T. Jung, *Nano Lett.*, 2016, **16**, 4508–4515.
9 V. S. Bhati, M. Hojamberdiev and M. Kumar, *Energy Rep.*, 2020, **6**, 46–62.

10 G. Li, Y. Fan, Q. Hu, D. Zhang, Z. Ma, Z. Cheng, X. Wang and J. Xu, *J. Alloys Compd.*, 2022, **906**, 163765.
11 X. Tian, X. Cui, T. Lai, J. Ren, Z. Yang, M. Xiao, B. Wang, X. Xiao and Y. Wang, *Nano Mater. Sci.*, 2021, **3**, 390–403.
12 C. Dong, R. Zhao, L. Yao, Y. Ran, X. Zhang and Y. Wang, *J. Alloys Compd.*, 2020, **820**, 153194.
13 H. Mayer, *Atmos. Environ.*, 1999, **33**, 4029–4037.
14 J. Pisk, D. Agustin, V. Vrdoljak and R. Poli, *Adv. Synth. Catal.*, 2011, **353**(16), 2910–2914.
15 J. Pisk, J. C. Daran, R. Poli and D. Agustin, *J. Mol. Catal. A:Chem.*, 2015, **403**, 52–63.
16 V. Lagostina, F. Carniato, D. Esteban-Gómez, C. Platas-Iglesias, M. Chiesa and M. Botta, *Inorg. Chem. Front.*, 2023, **10**, 1999–2013.
17 Y.-J. Zhang, L. Yin, J. Li, Z.-B. Hu, Z.-W. Ouyang, Y. Song and Z. Wang, *RSC Adv.*, 2020, **10**, 12833–12840.
18 R. Nickisch, W. M. de Vos, M. A. R. Meier and M. Irshad Baig, *ACS Appl. Polym. Mater.*, 2023, **5**, 7240–7251.
19 M.-Q. Yu, C.-Y. Yang, L.-J. Dong, Y. Yan, Y.-J. Feng, Z. Chen, H.-P. Xiao, H.-Y. Wang and J.-Y. Ge, *Inorg. Chem.*, 2024, **63**, 19287–19298.
20 E. Spain, S. Carrara, K. Adamson, H. Ma, R. O'Kennedy, L. De Cola and R. J. Förster, *ACS Omega*, 2018, **3**, 17116–17124.
21 İ. Koçak and F. Pekdemir, *J. Electrochem. Soc.*, 2023, **170**, 066501.
22 J. López-Molino and P. Amo-Ochoa, *ChemPlusChem*, 2020, **85**(7), 1564–1579.
23 X. Y. Xu, H. N. Xiao, Y.-M. Xu and M. J. Zhang, *Spectrochim. Acta, Part A*, 2012, **95**, 427–434.
24 X. Liu, W. Sun, L. Zou, Z. Xie, X. Li, C. Lu, L. Wang and Y. Cheng, *Dalton Trans.*, 2012, **41**, 1312–1319.
25 J. Jia, Y. Tian and Z. Li, *Synth. Met.*, 2011, **161**, 1377–1382.
26 C.-W. Zhao, J. P. Ma, Q.-K. Liu, X. R. Wang, Y. Liu, J. Yang, J.-S. Yang and Y.-B. Dong, *Chem. Commun.*, 2016, **52**, 5238–5241.
27 N. G. Utkarsha, A. Kushwaha, M. Kwoka, R. Kumar and M. Kumar, *J. Mater. Chem. A*, 2024, **12**, 5642–5667.
28 A. Sharmaa and C. Sekhar Rout, *J. Mater. Chem. A*, 2021, **9**, 18175–18207.
29 J. Sarjanović, M. Stojić, M. Rubčić, L. Pavić and J. Pisk, *Materials*, 2023, **16**, 1064.
30 J. Sarjanović, M. Cader, E. Topić, M. Razum, D. Agustin, M. Rubčić, L. Pavić and J. Pisk, *Mater. Adv.*, 2024, **5**, 9391–9402.
31 J. Sarjanović, E. Topić, M. Rubčić, L. A. Dubraja, L. Pavić and J. Pisk, *J. Mater. Chem. C*, 2024, **12**, 4013–4025.
32 S. Gupta, M. V. Kirillova, M. Fatima Guedes da Silva and A. J. L. Pombeiro, *Appl. Catal., A*, 2013, **82**, 460–461.
33 I. Syiemlieh, M. Asthana and R. A. Lal, *Appl. Organomet. Chem.*, 2019, **33**, e4984.
34 I. Syiemlieh, M. Asthana, S. D. Kurbah and R. A. Lal, *Polyhedron*, 2019, **170**, 202.
35 S. Gupta, M. V. Kirillova, M. Fatima, C. Guedes da Silva, A. J. L. Pombeiro and A. M. Kirillov, *Inorg. Chem.*, 2013, **52**, 8601.
36 H. Hosseini-Monfared, N. Asghari-Lalami, A. Pazio, K. Wozniak and C. Janiak, *Inorg. Chim. Acta*, 2013, **406**, 241.
37 D. Liu, Z. Chen, W. Huang, S. Qin, L. Jiang, S. Zhou and F. Liang, *Inorg. Chim. Acta*, 2013, **400**, 179.
38 J. Shi, Y. Wei, Y. Zhang, J. Tang, H. Bian, Q. Yu and F. Huang, *Polyhedron*, 2019, **162**, 81–90.
39 Z. H. Chohan, M. A. Farooq, A. Scozzafava and C. T. Supuran, *J. Enzyme Inhib. Med. Chem.*, 2002, **17**, 1–7.
40 K. J. Ardila-Fierro and J. G. Hernandez, *ChemSusChem*, 2021, **14**, 2145–2162.
41 T. Welton, *Proc. R. Soc.*, 2015, **471**, 20150502.
42 A. Bafti, M. Razum, E. Topić, D. Agustin, J. Pisk and V. Vrdoljak, *Mol. Catal.*, 2021, **512**, 111764.
43 J. Pisk, M. Šušković, E. Topić, D. Agustin, N. Judaš and L. Pavić, *Int. J. Mol. Sci.*, 2024, **25**, 4859.
44 J. P. Thielemann, J. Krohnert and C. Hess, *J. Phys. Chem.*, 2010, **114**, 17092–17098.
45 S. Mrkonja, M. Pajski, E. Topić, D. Agustin and J. Pisk, *Eur. J. Inorg. Chem.*, 2024, e202400350.
46 I. Sheikhshoaie, V. Langer and S. A. Yasrebi, *Acta. Cryst.*, 2011, **E67**, m839–m840.
47 J. R. Macdonald and W. B. Johnson, *Fundamentals of Impedance Spectroscopy*, John Wiley & Sons, Inc., 2018.
48 N. Bonanos, P. Pissis and J. R. Macdonald, *Impedance Spectroscopy of Dielectrics and Electronic Conductors*, John Wiley & Sons, Inc., 2012.
49 V. Kojić, M. Bohač, A. Bafti, L. Pavić, K. Salamon, T. Čižmar, D. Gracin, K. Juraić, M. Leskovac, I. Capan and A. Gajović, *Materials*, 2021, **14**, 4594.
50 M. Mustapić, A. Bafti, Z. Glumac, L. Pavić, Ž. Skoko, S. Šegota, T. Klaser, R. Nedeljković, M. K. Masud and A. A. Alothman, *et al.*, *Cellulose*, 2023, **30**, 1149–1169.
51 S. Roy, A. Dey, M. G. B. Drew, P. P. Ray and S. Chattopadhyay, *New J. Chem.*, 2019, **43**, 5020–5031.
52 R. Saha and C. J. Gomez Garcia, *Chem. Soc. Rev.*, 2024, **53**, 9490–9559.
53 J. C. Sancho-García, A. J. Pérez-Jiménez, Y. Oliver and J. Cornil, *Phys. Chem. Chem. Phys.*, 2010, **12**, 9381–9388.
54 N. S. Schauser, P. M. Richardson, A. Nikolaev, P. Cooke, G. A. Kliegle, E. M. Susca, K. Johnson, H. Wang, J. Read de Alaniz, R. Clément and R. A. Segalman, *Mol. Syst. Des. Eng.*, 2021, **6**, 1025.
55 S. G. Keskin, M. L. Mejia, A. H. Cowley and B. J. Holliday, *Macromol. Chem. Phys.*, 2018, **219**(22), 1800262.
56 E. A. Dmitrieva, I. A. Chepurnaya, M. P. Karushev and A. M. Timonov, *Russ. J. Electrochem.*, 2019, **55**, 1285–1294.
57 R. Saha, K. Gupta and C. J. Gomez Garcia, *Cryst. Growth Des.*, 2024, **24**, 2235–2265.
58 M. T. Nguyen, R. A. Jones and B. J. Holliday, *Macromolecules*, 2017, **50**, 872–883.
59 K. Saha, B. Dutta, P. Das, A. Chandra, A. Samantha, S. R. Jana, S. Naskar, R. Saha, P. P. Ray and C. Sinha, *Dalton Trans.*, 2025, **54**, 3346–3361.
60 C. M. Ngue, K. Fu Ho, B. Sainbileg, E. Batsaikhan, M. Hayashi, K. Yi Lee, R. San Chen and M. Kit Leung, *Chem. Sci.*, 2023, **14**, 1320–1328.

61 A. M. Laera and M. Penza, *Chemosensors*, 2024, **12**, 78.
62 R. Boroujerdi, A. Abdelkader and R. Paul, *Nano-Micro Lett.*, 2020, **12**, 33.
63 A. Leo, A. M. Monteduro, S. Rizzato, A. Milone and G. Maruccio, *Sensors*, 2022, **22**, 2742.
64 A. Benali, S. Azizi, M. Bejar, E. Dhahri and M. F. P. Graca, *Ceram. Int.*, 2014, **40**, 14367–14373.
65 P. X. Zhao, Y. Tang, J. Mao, Y. X. Chen, H. Song, J. W. Wang, Y. Song, Y. Q. Liang and X. M. Zhang, *J. Alloys Compd.*, 2016, **674**, 252–258.
66 I. Panžić, A. Bafti, F. Radovanoviić-Perić, D. Gašparić, Z. Shi, A. Borenstein and V. Mandić, *Appl. Sci.*, 2015, **15**, 2552.
67 A. Mhamdi, A. Labidi, B. Souissi, M. Kahlaoui, A. Yumak, K. Boubaker, A. Amlouk and A. Amlouk, *J. Alloys Compd.*, 2015, **639**, 648–658.
68 B. Abdelaoui, A. Benali, M. Bejar, E. Dhahri, M. P. Graça, M. A. Valente, L. Peng and J. Wu, *Colloids Surf., A*, 2024, **690**, 133789.
69 A. Lozančić, S. Renka, D. Barišić, S. Burazer, K. Molčanov, D. Pajić and M. Jurić, *Inorg. Chem.*, 2023, **62**, 9418–9428.
70 A. Lozančić, S. Burazer, S. Renka, K. Molčanov, L. Molčanov and M. Jurić, *ChemEngChem*, 2024, **26**, 1892–1901.
71 M. Aleksanyan, A. Sayunts, G. Shahkhatuni, Z. Simonyan, G. Shahnazaryan and V. Aroutiounian, *Chemosensors*, 2022, **10**, 245.
72 H. Shen, L. Li and D. Xu, *RSC Adv.*, 2017, **7**, 33098.
73 A. Sherma, S. B. Eadi, H. Noothalapati, M. Otyepka, H.-D. Lee and K. Jayaramulu, *Chem. Soc. Rev.*, 2024, **53**, 2530.
74 J. Li, H. Zhao, Y. Wang and Y. Zhou, *Sens. Diag.*, 2024, **3**, 336.
75 P. Karthick Kannan and R. Saraswathi, *Talanta*, 2014, **129**, 545–551.
76 A. Sharma and C. S. Rout, *J. Mater. Chem. A*, 2021, **9**, 18175–18207.
77 K. Phasuksom, W. Prissanaroon-Ouajai and A. Sirivat, *Sens. Actuators, B*, 2018, **262**, 1013–1023.
78 K. Mukherjee, C. E. Ekuma, Y. Zhao, A. Maikap, S. Najmaei and M. E. Zaghloul, *ChemPlusChem*, 2019, **84**, 387–391.
79 Z. Zhang, L. Zhang, J. Liu, Y. Zheng, W. Ren, Y. Xu and W. Weng, *Mater*, 2024, **7**, 104405.
80 S. Lin, Y. Li, W. Liu, Y. Zhang, H. Wang, X. Zhao, Y. Chen, Y. Zhang and L. Wang, *J. Phys. Chem. Lett.*, 2024, **15**, 9831–9837.
81 N. K. Chowdhury and B. Bhowmik, *Nanoscale Adv.*, 2021, **3**, 73–93.
82 T. Shinkai, J. K. C. N. Agutaya, B. Manna, M. Boepple, M. Iwai, K. Masumoto, K. Koga, K. Kawanami, Y. Nakamura, A. T. Quitain, K. Suematsu, Y. Inomata, N. Barsan and T. Kida, *J. Mater. Chem. A*, 2024, **12**, 7564–7576.
83 T. Lu, A. Adiraju, A. Lyu, Z. Cui, G. Shi, A. Al-Hamry, I. A. Pašti and O. Kanoun, *Emergent. Mater.*, 2025, **8**, 2815–2829.
84 A. Sharma, S. B. Eadi, H. Noothalapati, M. Otyepka, H. D. Lee and K. Jayaramulu, *Chem. Soc. Rev.*, 2024, **53**, 2530–2577.
85 M. Wang, Z. Zhang, H. Zhong, X. Huang, W. Li, M. Hambsch, P. Zhang, Z. Wang, P. S. Petkov, T. Heine, S. C. B. Mannsfeld, X. Feng and R. Dong, *Angew. Chem., Int. Ed.*, 2021, **60**, 18666–18672.
86 G. Feng, Z. Liu, P. Chen and H. Lou, *RSC Adv.*, 2014, **4**, 49924–49929.
87 R. Pandeeswari and B. G. Jeyaprakash, *Sens. Actuators, B*, 2014, **195**, 206–214.
88 L. Peng, P. Qin, Q. Zeng, H. Song, M. Lei, J. J. N. Mwangi, D. Wang and T. Xie, *Sens. Actuators, B*, 2011, **160**, 39–45.
89 Rigaku Oxford Diffraction. CrysAlisPro Software System, Versions 1.171.42.49, 1.171.41.92a, 1.171.41.93a and 1.171.42.53a, Rigaku Oxford Diffraction, Oxford, UK, 2020.
90 G. M. Sheldrick, *Acta Crystallogr., Sect. A: Found. Adv.*, 2015, **71**, 3–8.
91 G. M. Sheldrick, *Acta Crystallogr., Sect. C: Struct, Chem*, 2015, **71**, 3–8.
92 O. V. Dolomanov, L. J. Bourhis, R. J. Gildea, J. A. K. Howard and H. Puschmann, *J. Appl. Cryst.*, 2009, **42**, 339–341.
93 A. L. Spek, *Acta Crystallogr.*, 2009, **D65**, 148–155.
94 C. F. Macrae, I. Sovago, S. J. Cottrell, P. T. A. Galek, P. McCabe, E. Pidcock, M. Platings, G. P. Shields, J. S. Stevens, M. Towler and P. A. Wood, *J. Appl. Crystallogr.*, 2020, **53**, 226–235.
95 A. D. Becke, *J. Chem. Phys.*, 1993, **98**, 5648–5652.
96 M. J. Frisch, G. W. Trucks, H. B. Schlegel, G. E. Scuseria, M. A. Robb, J. R. Cheeseman, G. Scalmani, V. Barone, B. Mennucci, G. A. Petersson, H. Nakatsuji, M. Caricato, X. Li, H. P. Hratchian, A. F. Izmaylov, J. Bloino, G. Zheng, J. L. Sonnenberg, M. Hada, M. Ehara, K. Toyota, R. Fukuda, J. Hasegawa, M. Ishida, T. Nakajima, Y. Honda, O. Kitao, H. Nakai, T. Vreven, J. A. Montgomery, J. E. Peralta, F. Ogliaro, M. Bearpark, J. J. Heyd, E. Brothers, K. N. Staroverov, R. Kobayashi, J. Normand, K. Raghavachari, A. Rendell, J. C. Burant, S. S. Iyengar, J. Tomasi, M. Cossi, N. Rega, N. J. Millam, M. Klene, J. E. Knox, J. B. Cross, V. Bakken, C. Adamo, J. Jaramillo, R. Gomperts, R. E. Stratmann, O. Yazyev, A. J. Austin, R. Cammi, C. Pomelli, W. J. Ochterski, R. L. Martin, K. Morokuma, V. G. Zakrzewski, G. A. Voth, P. Salvador, J. J. Dannenberg, S. Dapprich, A. D. Daniels, Ö. Farkas, J. B. Foresman, J. V. Ortiz, J. Cioslowski and D. J. Fox, *Gaussian 19, Revisiom C.01*, Gaussian, Inc, Wallingford CT, 2009.
97 T. H. Dunning and P. J. Hay, Gaussian Basis Sets for Molecular Calculations, in *Methods of Electronic Structure Theory, Modern Theoretical Chemistry*, ed. Schaefer, H. F., Springer, Boston, MA, 1977, vol. 3.
98 P. Fuentealba, H. Preuss, H. Stoll and L. Von Szentpály, *Chem. Phys. Lett.*, 1982, **89**, 418–422.
99 D. Andrae, U. Häußermann, M. Dolg, H. Stoll and H. Preuß, *Theoret. Chim. Acta*, 1990, **77**, 123–141.
100 S. Grimmie, J. Antony, S. Ehrlich and H. Krieg, *J. Chem. Phys.*, 2010, **132**, 154104.
101 CCDC 2434680: Experimental Crystal Structure Determination, 2025, DOI: 10.5517/ccdc.csd.cc2mqh2y.